Geochemistry Geophysics Geosystems G3

Article
Volume 12, Number 7
12 July 2011
Q07005, doi:10.1029/2011GC003665
ISSN: 1525-2027

Published by AGU and the Geochemical Society

On the location of plumes and lateral movement of thermochemical structures with high bulk modulus in the 3-D compressible mantle

Eh Tan
Computational Infrastructure for Geodynamics, California Institute of Technology, Pasadena, California 91125, USA

Now at Institute for Geophysics, University of Texas at Austin, Austin, Texas 78758, USA (tan2@mail.utexas.edu)

Wei Leng
Department of Physics, University of Colorado at Boulder, Boulder, Colorado 80309, USA

Now at Seismological Laboratory, California Institute of Technology, Pasadena, California 91125, USA

Shijie Zhong
Department of Physics, University of Colorado at Boulder, Boulder, Colorado 80309, USA

Michael Gurnis
Computational Infrastructure for Geodynamics, California Institute of Technology, Pasadena, California 91125, USA

Now at Seismological Laboratory, California Institute of Technology, Pasadena, California 91125, USA

[1] The two large low shear velocity provinces (LLSVPs) at the base of the lower mantle are prominent features in all shear wave tomography models. Various lines of evidence suggest that the LLSVPs are thermochemical and are stable on the order of hundreds of million years. Hot spots and large igneous province eruption sites tend to cluster around the edges of LLSVPs. With 3-D global spherical dynamic models, we investigate the location of plumes and lateral movement of chemical structures, which are composed of dense, high bulk modulus material. With reasonable values of bulk modulus and density anomalies, we find that the anomalous material forms dome-like structures with steep edges, which can survive for billions of years before being entrained. We find that more plumes occur near the edges, rather than on top, of the chemical domes. Moreover, plumes near the edges of domes have higher temperatures than those atop the domes. We find that the location of the downwelling region (subduction) controls the direction and speed of the lateral movement of domes. Domes tend to move away from subduction zones. The domes could remain relatively stationary when distant from subduction but would migrate rapidly when a new subduction zone initiates above. Generally, we find that a segment of a dome edge can be stationary for 200 million years, while other segments have rapid lateral movement. In the presence of time-dependent subduction, the computations suggest that maintaining the lateral fixity of the LLSVPs at the core-mantle boundary for longer than hundreds of million years is a challenge.

Components: 7300 words, 7 figures, 5 tables.

Keywords: LLSVP; plume; thermochemical convection.

Index Terms: 8121 Tectonophysics: Dynamics: convection currents, and mantle plumes; 8124 Tectonophysics: Earth's interior: composition and state (1212, 7207, 7208, 8105); 8137 Tectonophysics: Hotspots, large igneous provinces, and flood basalt volcanism.

Received 18 April 2011; **Revised** 17 May 2011; **Accepted** 18 May 2011; **Published** 12 July 2011.

Tan, E., W. Leng, S. Zhong, and M. Gurnis (2011), On the location of plumes and lateral movement of thermochemical structures with high bulk modulus in the 3-D compressible mantle, *Geochem. Geophys. Geosyst.*, *12*, Q07005, doi:10.1029/2011GC003665.

1. Introduction

[2] The two large low shear velocity provinces (LLSVPs) at the base of lower mantle are prominent features in shear wave tomography models [*Masters et al.*, 2000; *Romanowicz*, 2003]. LLSVPs cover about 20% of the core-mantle boundary (CMB) by area [*Burke et al.*, 2008] and have high elevation, extending at least 500 km above the CMB [*Ni et al.*, 2002; *He and Wen*, 2009]. The shear wave velocity anomaly and bulk sound velocity anomaly of the LLSVPs are anticorrelated [*Masters et al.*, 2000; *Ishii and Tromp*, 2004]. Sharp transitions in shear wave velocity occur across the LLSVPs boundary [*Wen*, 2001; *Ni et al.*, 2002]. These observations suggest that the LLSVPs have a significant change in chemical composition compared to ambient mantle. The reconstructed eruption sites of large igneous provinces (LIPs) over past 200 million years (Myr) [*Burke and Torsvik*, 2004] and of Kimberlites over past 540 Myr [*Torsvik et al.*, 2010] spatially coincide with the present-day edges of LLSVPs. These observations suggest that (1) the LLSVPs are not short-term transient structures, but long-term stable ones and (2) the LLSVPs have no significant lateral drift over the past 200 Myr or longer. Moreover, if the LLSVPs are the source reservoir of the DUPAL geochemical anomaly [*Wen*, 2006], they must be older than 1–2 billion years (Gyr) [*Hofmann*, 1997].

[3] The stability of dense chemical structures against entrainment at the base of mantle has been extensively studied [*Tan and Gurnis*, 2007, and references therein]. The stability of the dense chemical structures is mainly controlled by the balance between net buoyancy (thermal and chemical effects combined) and plume-induced entrainment that tends to erode the chemical structures over time [*Sleep et al.*, 1988; *Davaille*, 1999; *Jellinek and Manga*, 2002; *Gonnermann et al.*, 2002; *Zhong and Hager*, 2003; *Nakagawa and Tackley*, 2004; *Huang*, 2008]. A net negative buoyancy of ~1% for the dense chemical structures may be needed for the structure to survive for 4.5 Gyr of the Earth's history, if the chemical density anomaly is constant with depth [*Zhong and Hager*, 2003]. One the other hand, such large net negative buoyancy will give the chemical structures a ridge-like shape in a vertical cross section and, more importantly, low elevation. Reconciling the observed high elevation of LLSVPs and the conceived longevity is difficult in dynamic models [*Ni et al.*, 2002]. Recently, it has been demonstrated in 2-D Cartesian models that if a different equation of state (EOS), from anomalous material with high bulk modulus and large density, is applied to the chemical structure, both high elevation and longevity can be achieved over wide range of parameters [*Tan and Gurnis*, 2005]. In this study, we will extend the EOS concept of high bulk modulus material to 3D spherical models, and explore its effects on the location and lateral movement of plumes and LLSVPs.

[4] The locations of hot spots, when projected down to the lowermost mantle, tend to cluster around the edges of LLSVPs, where the shear wave velocity gradient is the largest [*Thorne et al.*, 2004; *Torsvik et al.*, 2006]. In isochemical models, plume roots commonly locate near the edges of slabs [*Lenardic and Kaula*, 1994; *Lowman and Jarvis*, 1996; *Tan et al.*, 2002], which have strong lateral temperature gradients at the CMB. However, in thermochemical models, plumes are more likely to root on crests of the chemical anomalies [*Jellinek and Manga*, 2002; *McNamara and Zhong*, 2005; *Deschamps and Tackley*, 2009]. In these models, the chemical anomalies form ridge-like structure with shallow slope toward the crest (Figure 1a). Warm mantle material rises along the slope and takes off as plumes at the ridge crests. In a map view, the plumes (and

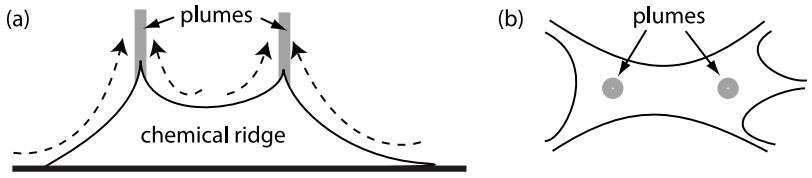

Figure 1. (a) A cross section of a ridge-like chemical structure. Plumes rise from the crests of the ridge. Dashed arrows show the direction of mantle flow. (b) In a map view, plumes are located well into the interior of the chemical structures.

hot spots) would be within, rather than on the edges, of the chemical anomaly (Figure 1b). Consequently, plumes do not cluster around the edges of chemical structures in most thermochemical models.

[5] The lateral movement of hot spots and LLSVPs is another interesting topic. The reconstructed eruption sites of LIPs [*Burke and Torsvik*, 2004] and Kimberlites [*Torsvik et al.*, 2010] spatially coincide with the present-day edges of LLSVPs at the CMB. These observations pose one important question. Are the LLSVPs stationary at CMB without significant lateral movement for the last 500 Myr or so? *McNamara and Zhong* [2004] found that mantle downwellings upon reaching the CMB tend to push around the chemical structures. Furthermore, *McNamara and Zhong* [2005] found that subduction history for the last 120 Myr plays an important role in organizing the LLSVPs to the present-day location. The question arises when it comes to whether it is possible to reconcile the observation of LIP eruption sites, which seems to be stationary relative to the edge of LLSVPs, with the general characteristic of dynamic models, which show the movement of LLSVPs due to the pushing effects of subduction.

[6] The presented study uses compressible convection models in 3-D spherical shell geometry, and represents one of the first studies on compressible convection with variable viscosity and material properties in such geometry. We will present a set of thermochemical models where the chemical structures survive entrainment for billions of years, with the top extending more than 500 km above CMB, and with plumes forming around the edges. Essentially, the material of chemical structure has a different EOS than the ambient mantle, due to higher bulk modulus and density. We observe the spatial correlation of plumes with the edges of chemical structures in the models. We also investigate the lateral movement of the chemical structures, especially how long they can remain stationary in one location, and try to reconcile the lateral movement with the proposed stationary from reconstructed LIP and Kimberlite eruption sites.

2. Methods

[7] We used the mantle convection code CitcomS v3.1 [*Zhong et al.*, 2000, 2008; *Tan et al.*, 2006, 2010] with one modification: the chemical density anomaly is allowed to change radially to simulate the effect of the bulk modulus anomaly [*Tan and Gurnis*, 2005]. The mantle is treated as an anelastic, compressible, viscous spherical shell under the Truncated Anelastic Liquid Approximation [*Ita and King*, 1994]. The (nondimensional) governing equations are:

$$\nabla \cdot (\rho_r \mathbf{u}) = 0, \tag{1}$$

$$-\nabla P + \nabla \cdot \underline{\tau} = (C\Delta\rho_{ch}/\alpha_0\Delta T - \rho_r \alpha T) g Ra \mathbf{e}_r, \tag{2}$$

$$\rho_r C_P \frac{\partial T}{\partial t} = -\rho_r C_P \mathbf{u} \cdot \nabla T + \nabla \cdot (k_T \nabla T) + Di(T + T_s)\rho_r \alpha g u_r + \frac{Di}{Ra} \underline{\tau} : \underline{\varepsilon} + \rho_r H, \tag{3}$$

where $\rho_r = \rho_r(r)$ is density; $\mathbf{u} = (u_\theta, u_\varphi, u_r)$ is the velocity vector; P is dynamic pressure; $\underline{\tau}$ is deviatoric stress tensor; C is the concentration (between 0 to 1) of the anomalous material; $\Delta\rho_{ch} = \Delta\rho_{ch}(r)$ is chemical density anomaly; α_0 is reference coefficient of thermal expansion (dimensional); ΔT is total temperature contrast (dimensional); $\alpha = \alpha(r)$ is the coefficient of thermal expansion; T is temperature; g is gravity; Ra is thermal Rayleigh number; $\mathbf{e}_r$ is the radial unit vector; C_P is heat capacity at constant pressure; t is time; k_T is thermal conductivity; Di is dissipation number; T_s is surface temperature; $\underline{\varepsilon}$ is strain rate tensor; H is internal heating.

[8] The constitutive relationship is:

$$\underline{\tau} = 2\eta\left(\underline{\varepsilon} - \frac{1}{3}(\nabla \cdot \mathbf{u})\underline{I}\right) = \eta\left(\nabla\mathbf{u} + (\nabla\mathbf{u})^T - \frac{2}{3}(\nabla \cdot \mathbf{u})\underline{I}\right), \tag{4}$$

Table 1. Values of Parameters Used in Models

Symbol	Value
Ra	1.376×10^9
Di	2.0
γ	2.667
T_s	0.1
r_{inner}	0.546
h	6.371×10^9 m
ρ_0	3600 kg/m^3
g_0	10 m/s^2
α_0	5×10^{-5} K^{-1}
ΔT	4000 K
κ_0	10^{-6} m^2/s
η_0	1.35×10^{21} Pa s
C_{P0}	1.593×10^3 J/kg/K
K_{S0}	3.058×10^{11} GPa

where η is the viscosity, and $\underline{I}$ is the identity tensor. The thermal Rayleigh number is defined as $Ra = \rho_0 g_0 \alpha_0 \Delta T h^3/\kappa_0\eta_0$, where ρ_0 is reference density; g_0 is reference gravity; h is the radius of the Earth; κ_0 is reference thermal diffusivity; η_0 is reference viscosity. The dissipation number is defined as $Di = \alpha_0 g_0 h/C_{P0}$, where C_{P0} is reference heat capacity at constant pressure. The values of various parameters are listed in Table 1. The numerical algorithm for solving the equations is presented in Appendix A. The Stokes solver is benchmarked with semi-analytical solution in Appendix B.

[9] The mantle is divided into 12 blocks. Each block is further subdivided into 64^3 elements, such that there are 3.15 million elements in total. The lateral grid spacing is about 0.5°. The radial grid spacing is 50 km at midmantle and gradually refined to 32 km near the top and bottom boundary. The grid has a nondimensional outer radius 1.0 and inner radius, r_{inner}, 0.546. The top and bottom boundaries are free slip and isothermal, with $T = 0$ and 1, respectively. The total angular momentum of the whole mantle is removed at every time step to prevent net rotation [*Zhong et al.*, 2008].

[10] The coefficient of thermal expansion decreases by a factor of 5 from surface to CMB [e.g., *Davies*, 1999, Table 7.3] and is parameterized by the equation

$$\alpha = \left(1 + 4\left(\frac{1-r}{1-r_{inner}}\right)^{0.8}\right)^{-1}. \quad (5)$$

Although the coefficient of thermal expansion changes only gently in the lowermost mantle, this profile destabilizes the chemical structures significantly.

[11] The initial temperature is uniformly 0.5 everywhere with a hot thermal boundary layer at the bottom. The density profile, ρ_1, of the ambient material and the hydrostatic pressure profile, P_H, are computed by integrating the nondimensional self-compression equation:

$$\begin{aligned} dP_H &= -\rho_1 g dz \\ d\rho_1 &= \frac{Di}{\gamma}\rho_1 dP_H \\ \rho_1 = 1, \quad P_H &= 0, \quad \text{at } r = 1 \end{aligned}, \quad (6)$$

where γ is the Gruneisen parameter $\gamma = \alpha_0 K_{S0}/\rho_0 C_{P0}$ and K_{S0} is the reference bulk modulus. Equation (6) is essentially the Adams-Williamson equation of state. Profiles of α, ρ_1, and P_H are shown in Figure 2a. Tracers are used to simulate different compositions [*McNamara and Zhong*, 2004]. More than 62.9 million tracers are randomly generated to fill the mantle. Tracers initially below $r = 0.63$ are considered anomalous with a different equation of state and a density profile ρ_2, which results in an initially flat dense layer at the base of the mantle. The anomalous material has a bulk modulus anomaly ΔK_s and a density anomaly $\Delta\rho_{CMB}$ at the CMB. The associated density profile is:

$$\begin{aligned} d\rho_2 &= \frac{Di}{\gamma}\frac{\rho_2}{1+\Delta K_S} dP_H \\ \rho_2 &= \rho_1 + \Delta\rho_{CMB} \text{ at } r = r_{inner} \end{aligned}. \quad (7)$$

The chemical density anomaly, $\Delta\rho_{ch} = \rho_1 - \rho_2$, is the density difference between the two materials and varies with depth or pressure.

[12] The viscosity is temperature and depth dependent following the equation

$$\eta = \eta(r)\exp\left[E\left(T_{ref} - T\right)\right], \quad (8)$$

where $\eta(r)$ determines four viscous layers: a high-viscosity lithosphere, a low-viscosity asthenosphere, a moderately high viscosity transition zone, and a high-viscosity lower mantle (Table 2). E is nondimensional activation energy with a value of 6.9, which leads to viscosity variations of 10^3 due to temperature change in the mantle. T_{ref} is a reference temperature and is set to 0.5. The combination of low-viscosity asthenosphere and high-viscosity lithosphere and lower mantle will promote long-wavelength convection structures [*Zhong et al.*, 2007; *Höink and Lenardic*, 2008]. The viscosity has a maximum and a minimum cutoff of 10^2 and 10^{-2}, respectively. The gravity, heat capacity, and thermal diffusivity are assumed constant. Note that the Rayleigh number, dissipation number and Gruneisen parameter appear to be larger than values used in

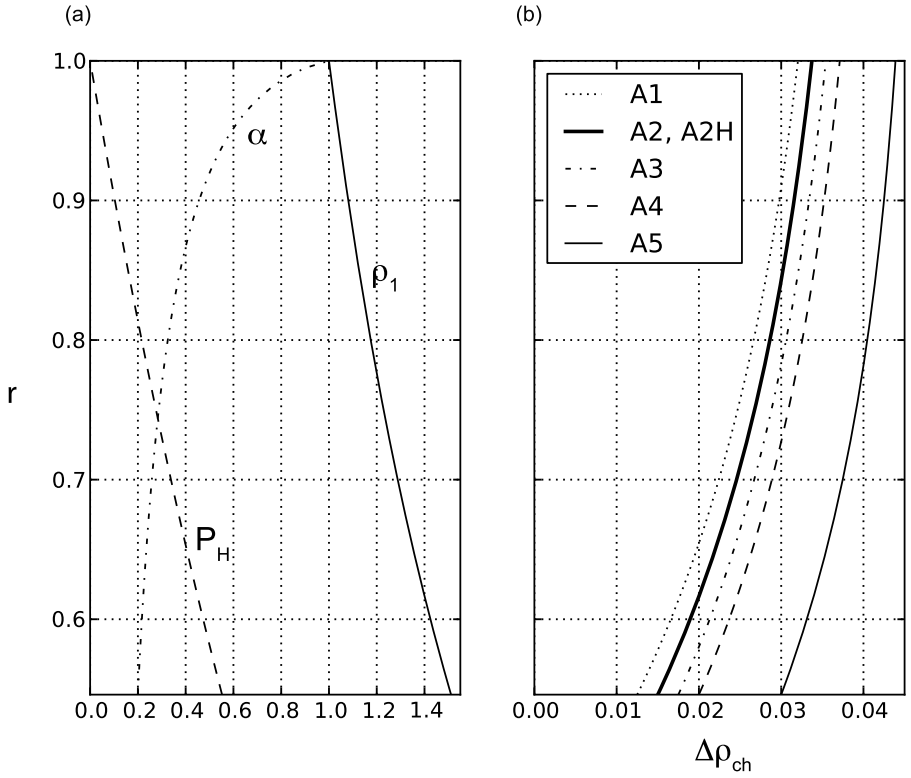

Figure 2. (a) Profiles of α, ρ_1, and P_H. (b) Profiles of $\Delta\rho_{ch}$ of all cases.

the literature (around 10^8, 0.5 and 1.0, respectively) because here they are nondimensionalized by the radius of the Earth, instead of by the thickness of the mantle, and the values of several parameters are taken from their values at the surface, instead of volume-averaged values. Nondimensionalizing by the radius of the Earth makes equations (2), (3), (6), and (7) very similar to the corresponding equations in Cartesian geometry.

3. Results

[13] To find models with stable chemical structures, we compute five models while varying $\Delta\rho_{CMB}$ with ΔK_s = 0.06, and one model with internal heating (Table 3). Profiles of $\Delta\rho_{ch}$ of all models are shown in Figure 2b. Note that all $\Delta\rho_{ch}$ profiles have positive slope, which is crucial to maintain the steep edges of chemical structures. All these models have *Ra* of 1.376×10^9 (Table 1). Models with small $\Delta\rho_{CMB}$ have unstable chemical layers (case A1). Models with moderate $\Delta\rho_{CMB}$ have stable dome-like chemical structures (cases A2, A2H, A3, A4). Models with even larger $\Delta\rho_{CMB}$ have stable ridge-like chemical structures (case A5).

[14] We will describe case A2 ($\Delta\rho_{CMB}$ = 0.015 and ΔK_s = 0.06) in more detail. This case has an average nondimensional root-mean-square (RMS) convective velocity of 2001 (equivalent to 0.98 cm/yr) and an average nondimensional surface heat flow $4\pi \times 20.1$ (equivalent to 36.9 TW) at ~3 Gyr of model time, such that its convective vigor is overall consistent with that for the Earth's mantle. The RMS velocity may be slightly lower than that of Earth, and hence the model time may be slightly longer than real time. However, the deviation should be small. The chemical anomaly in this case forms stable chemical structures that survive for about 4 Gyr of model time.

[15] The temperature field at 2965 Myr is shown in Figures 3a and 3b. Three largely isolated chemical domes with high temperature are in the lowermost mantle. Areas not occupied by chemical domes are

Table 2. Viscosity Layers Used in Models

Radius Range	Depth Range (km)	$\eta(r)$
0.985–1.0	0–95	10.0
0.936–0.985	95–410	0.3
0.89–0.936	410–700	1.0
r_{inner}–0.89	700–CMB	10.0

Table 3. Cases in This Study

Cases	$\Delta\rho_{CMB}$	H	Result
A1	0.0125	0	Unstable
A2	0.015	0	Domes
A2H	0.015	10C	Domes
A3	0.0175	0	Domes
A4	0.02	0	Domes
A5	0.03	0	Ridges

covered by remnants of subducted slabs. The chemical domes have very steep edges ($C = 0.5$ contours). Sometimes the slope even exceeds 90°. This is quite contrary to the shallow slope angle of ridge-like chemical structures. The steep edges have strong influence on the location of plumes, as will be discussed later. Bulk of the domes extends to 800 km elevation above CMB, but some portions can extend to 1200 km. The high elevation and steep edges of the domes are maintained by the dynamic balance between thermal and chemical anomalies [*Tan and Gurnis*, 2005]. Thermal anomaly dominates over chemical anomaly for bulk of the domes (Figure 3c). The positive buoyancy lifts the anomalous material high up in the mantle and keeps the edges at high angle. Due to the positive slope of $\Delta\rho_{ch}$ profile, the chemical density anomaly gets larger with higher r. At $r = 0.7$, the chemical anomaly dominants over the thermal anomaly, and the chemical dome is stabilized at this height. Several plumes are visible in Figure 3b, e.g., at −40°, 85°, 100°, and 160° longitudes. The plume at 85° longitude originates from the CMB and is warmer than the plume at 100°, which originates from the top of a dome. We find that plumes of different origins have different temperature in all cases.

[16] Comparing cases A2, A3, A4, and A5, we found that the shape of chemical structures systematically changes as $\Delta\rho_{CMB}$ increases (Figure 4). The edges of the chemical structures become less steep, and the elevation of the chemical structures become lower, as $\Delta\rho_{CMB}$ increases. The cross sections of the chemical structures change from steep-sloped domes (case A2, Figure 3b), to domes where the slope is gentle at the CMB but becomes steeper with height (case A4, Figure 4a), and finally to ridge-like structures with gentle slopes throughout the edges (case A5, Figure 4b). The average temperature inside the chemical structures increases to compensate the chemical buoyancy.

[17] We plotted the location of plumes (defined as thermal anomaly larger than a threshold temperature) at 1000 km depth and the location of chemical domes at 2800 km depth for case A2 (Figure 5). Plumes are defined by two temperature thresholds: general plumes (blue contours) with $T > 0.5$ and strong plumes (green contours) with $T > 0.55$. Most strong plumes are connected directly to the CMB. We examined each strong plume individually. Strong plumes either rise as distinct conduits (like the plume at 85° longitude in Figure 3b) or rise along the edge of domes (not shown in this cross section, but a similar plume can be found in Figure 4a on the right side of the dome). When plotted in a map view, only weak plumes (i.e., $0.55 > T > 0.5$) are *on top of* the chemical domes (defined as: inside the $C = 0.5$ contours in a map view, but more than 5° away from the contours).

[18] The steepness of edges strongly affects the location of plumes. We measured the distance of strong plumes to the edges of chemical structures. To be consistent with seismic observations, the measurement is taken when the chemical structures cover ~20% of CMB. The criteria of strong plumes are adjusted to keep the number of plumes similar to case A2. The results are summarized in Table 4. The clustering of strong plumes around edges is common in all cases. The edges and ±5° surroundings cover only 5% to 11% of CMB. However, we found that about 43% to 48% of strong plumes are within 5° distance to the edges, and none or few strong plumes are on top of the domes. Cases with larger $\Delta\rho_{CMB}$ have more strong plumes on top of the chemical structures.

[19] Case A2H is similar to case A2, but the anomalous material is assumed to be enriched in radiogenic elements. The internal heating rate is proportional to C, the concentration of anomalous material. The chemical structures still have dome-like shapes and steep edges. The additional internal heating raises the internal temperature of chemical domes slightly and increases the abundance of plumes near the edges of chemical domes. The average heat flow is increased to $4\pi \times 21.3$, ~10% of which comes from internal heating. We found that 67% of strong plumes are within 5° distance to the edges of domes, with only one of them on top of domes.

[20] We then investigated the lateral movement of chemical domes. The amount of lateral movement in the models is difficult to quantify. We could only describe it qualitatively. All cases with stable chemical domes (cases A2, A2H, A3, A4) share similar characteristics. We will use case A2 as an example. The composition field of case A2 at 2400 km depth of 4 different time steps, with an interval ~200 Myr,

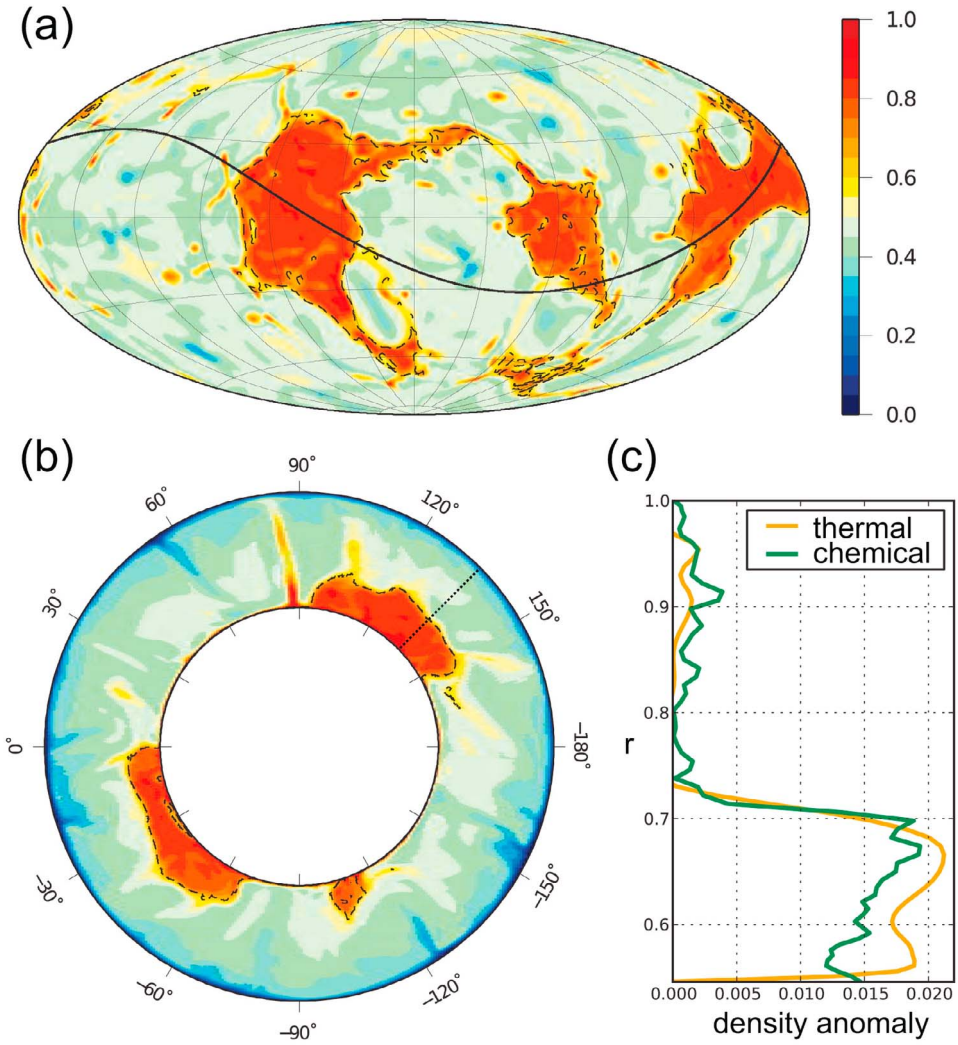

Figure 3. Temperature field and composition contour ($C = 0.5$, dashed line) at 2965 Myr of case A2. (a) At 2400 km depth, centered at 180° longitude. (b) Along a great circle cross section. (c) Thermal and chemical density anomaly profiles at 135° in Figure 3b. The magnitude of thermal density anomaly is $\rho_1\alpha(T - T_{avg})\alpha_0\Delta T$, where T_{avg} is the horizontal-averaged temperature profile. The chemical density anomaly is $\Delta\rho_{ch}C$.

is shown in Figure 6. The chemical domes have significant lateral movement over the 800 Myr. We found that the location of sheet-like cold downwellings (subduction zones) controls the direction and speed of the movement of domes. With free-slip surface boundary conditions in our models, the geometry and lateral position of downwellings change with time. Old subduction zones diminish while new ones initiate. Sometimes, a new subduction zone initiates above the chemical domes. The newly subducted slab, while still within the midmantle, creates a downwelling flow below. This flow suppresses the height of the chemical domes and pushes them aside, causing rapid lateral movement, like region S1 from Figures 6a to 6b to 6c, region S2 from Figures 6b to 6c, and region S3 from Figures 6c to 6d. On the other hand, when part of a chemical dome is distant from subduction zones, it can remain relatively stationary, e.g., edge E1 from Figures 6a to 6b and edge E2 from Figures 6c to 6d. A false sense of apparent fixity is also possible. For example, edge E3 is in close proximity to part of edge E1, although the whole chemical dome has moved significantly during the time span.

4. Discussions

[21] The steep edges of chemical domes in our models are distinctive from gentle edges of ridge-like chemical structures in other models. Using a

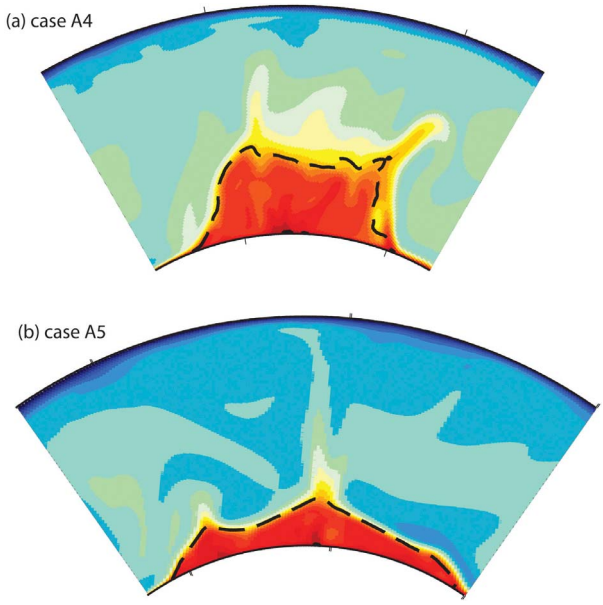

Figure 4. (a) Temperature cross section of case A4. The edges of the chemical structure are not as steep as those in case A2. A plume rises along the right edge of the chemical structure. (b) Temperature cross section of case A5. The edges have very gentle slope. Plumes rising from the crests are far away from the left/right edges. The color scale is the same as in Figure 2.

material with higher bulk modulus than ambient mantle is crucial in generating stable, steep-edged, high-elevation chemical structures [*Tan and Gurnis*, 2007]. Seismic waveform studies have found steep edges in several parts of LLSVPs [*Ni et al.*, 2002; *To et al.*, 2005; *Wang and Wen*, 2007; *He and Wen*, 2009]. The high elevation of LLSVPs suggests that they are nearly neutrally buoyant. We suggest that the LLSVPs are made of high bulk modulus material, which is implied by their observed positive anomaly in bulk sound velocity, and we do find that the dynamical consequence (i.e., the steep edges and high elevation) of high bulk modulus is consistent with the seismic observations of LLSVPs.

[22] We found a spatial correlation between the location of strong plumes and the edges of chemical domes. In our models, about half of strong plumes are around the edges of domes. We attribute the correlation to two features: (1) The area of slabs is generally devoid of plumes and (2) plumes on top of chemical domes are usually weaker. Feature 1 is straightforward. The cold temperature in the downwelling region inhibits plume formation. The large-scale circulation pushes plumes toward the upwelling region [*Zhong et al.*, 2000; *Jellinek et al.*, 2003]. In our models, the CMB is mostly covered by chemical domes and slab remnants. Absent from slab regions, plumes are more likely to be found around the edges and on top of chemical domes. Feature 2 deserves more discussion. We found that plumes above the chemical domes have their root on top of chemical domes and drain heat from the domes, which have lower temperature than the CMB. Hence, these plumes have lower temperature than plumes rooted on the CMB. These weak plumes are more easily deflected by large-scale mantle flow, more likely blocked by the 660 km discontinuity, and less likely to reach the surface and produce hot spots. An example of one such weak plume atop the African LLSVP that has not penetrated to the surface has been imaged recently [*Sun et al.*, 2010]. When internal heating due to enriched material is incorporated, we found that even higher percentages (67%) of strong plumes are near the edges of chemical domes, due to more heat available from the domes. Many geochemical arguments suggest that there is a hidden geochemical reservoir enriched with radiogenic elements in the deep mantle [*Allègre et al.*, 1996; *Hofmann*, 1997], and LLSVPs are the primary candidate of such a reservoir. Combining these arguments, we suggest that the locations of surface hot spots, when projected downward, are more likely to be near the edges of, rather than on top of, LLSVPs. A similar study by *Steinberger and Torsvik* [2011], which use the plate reconstruction since 300 Myr ago as the surface boundary condition, found that plumes are pushed by subducted slabs toward the edges of LLSVPs.

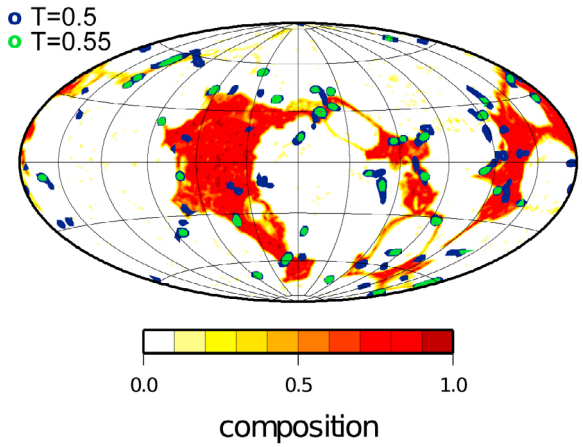

Figure 5. The locations of plumes at upper mantle plotted on top of the composition field at 2800 km depth. The blue contours are plumes (T = 0.5) at 1000 km depth, and the green contours are strong plumes (T = 0.55) at 1000 km depth.

Table 4. Distance of Plumes to Edges of Chemical Domes

Case	Criterion of Strong Plumes	Number of Strong Plumes	Number of Strong Plumes Within 5° of Edges	% of Strong Plumes Within 5° of Edges	Strong Plumes on Top of Domes	Area of ±5° Around Edges (% of CMB)
A2	$T > 0.55$	46	20	43.5	0	11.42
A2H	$T > 0.56$	48	32	66.7	1	6.29
A3	$T > 0.55$	48	21	43.8	3	9.94
A4	$T > 0.505$	47	23	48.9	5	5.84
A5	$T > 0.415$	50	28	56.0	22	5.31

[23] The anticorrelation of the locations of chemical structures and subduction zones in models has been long known [e.g., *Gurnis*, 1986; *McNamara and Zhong*, 2005]. The chemical domes are constantly being pushed away by subducted slabs. When subduction geometry is stable, the slab push forces exerted on a dome might balance each other, and the dome could remain stationary. When the geometry of subduction zones changes, the slab push forces change, and a dome would adjust its location accordingly. Given the frequency of subduction initiation and termination in our model and that inferred from the geological record [*Gurnis et al.*, 2004], we found that maintaining the spatial stability of the LLSVPs at the CMB for hundreds of million years is challenging in the Earth's mantle with time-dependent subduction. For example, *Zhang et al.* [2010] found that the African LLSVP may not be at its current location during the Pangea in their thermochemical convection models that consider the convergence and subduction between Laurussia and Gondwana before Pangea formation in the African hemisphere.

[24] Our result does not necessarily conflict with the correlations of seismic structures and reconstructed LIPs [*Burke and Torsvik*, 2004] and Kimberlites of [*Torsvik et al.*, 2010]. LIPs and Kimberlite eruptions are rare events. The reconstructed eruption sites are sparse in time and space, particularly before 200 Myr. For example, there is no LIP preserved near the western edge of the Pacific LLSVP. One cannot rule out large lateral movement for the western edge of the Pacific LLSVP

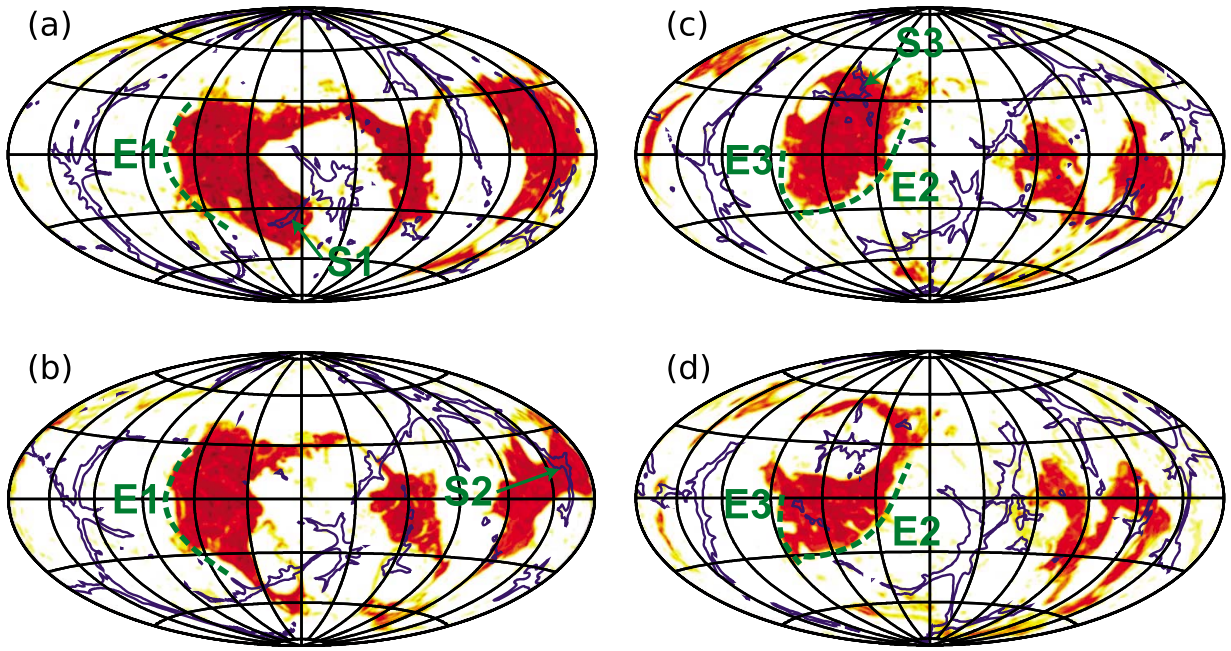

Figure 6. Lateral movement of the chemical structures and location of downwellings of case A2 at (a) 2737 Myr, (b) 2965 Myr, (c) 3175 Myr, and (d) 3361 Myr. The blue contours show the cold downwellings ($T = 0.3$) at 130 km depth. The background shows the composition field at 2400 km depth. The color scale of composition field is the same as in Figure 4.

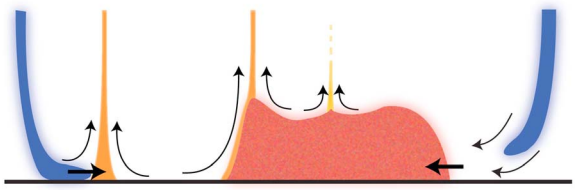

Figure 7. A schematic diagram showing possible interaction between slabs, plumes, and LLSVPs. Slabs push plumes toward LLSVPs. Some plumes rise along the steep edges of LLSVPs. Some weaker plumes that root on top of LLSVPs may not reach surface. Slabs can induce large-scale flow to push LLSVPs aside.

during the past 200 Myr. On the other hand, we do find that in regions distal from subduction zones, portions of the chemical domes could be stationary for a few hundred million years.

[25] In summary, we will use a diagram to illustrate possible interactions between LLSVPs, plumes, and slabs (Figure 7). Plumes are pushed away from downwelling regions and toward LLSVPs by slabs. A large percentage of plumes will be around the edges of LLSVPs and rise along the steep edges of LLSVPs. Some weaker plumes rooted on top of LLSVPs may not rise to the surface. When LLSVPs are nearby subducted slabs, they would be pushed aside.

5. Conclusions

[26] Assuming different bulk modulus, density, and equation of states for the chemically distinct materials above the CMB, we investigated the relation of the dense chemical structures with subducted slabs and plumes. We presented models of stable dome-like chemical structures with reasonable values of bulk modulus and density anomalies. These chemical domes have steep edges. We found that most plumes occur near the edges of the domes, while that few plumes occur on top of the domes or distal from the domes. The plumes near the edges of domes also have higher temperature than those on top of domes. We found that the location of subduction controls the direction and speed of dome movement. Domes tend to move away from subduction zones. The domes could remain relatively stationary when distant from subduction, but would migrate rapidly when new subduction zone initiated above. Our studies suggest that maintaining the spatial stability of the LLSVPs at the CMB for hundreds of million years is a challenge in the Earth's mantle with time-dependent and dynamic subduction.

Appendix A: Numerical Algorithms

[27] The discretization for compressible Stokes equations is based on the method of *Zhong et al.* [2000, Appendix A]. The continuity equation (1) can be rearranged as

$$\nabla \cdot \mathbf{u} + \frac{1}{\rho_r}\frac{d\rho_r}{dr}u_r = 0. \tag{A1}$$

[28] After discretization, the continuity equation (A1) and momentum equation (2) become:

$$(\mathbf{G}^{\mathbf{T}} + \mathbf{B})u = 0, \tag{A2}$$

$$\mathbf{K}u + \mathbf{G}p = f, \tag{A3}$$

where u is the velocity; p the dynamic pressure; $\mathbf{G}$ is the gradient operator, whose transpose $\mathbf{G}^{\mathbf{T}}$ is the divergence operator; $\mathbf{B}$ is a constant matrix due to the second term in equation (A1); $\mathbf{K}$ is the stiffness matrix; f is the force vector.

[29] For the incompressible cases, $\mathbf{B}$ is zero. Equation (A3) can be transformed by premultiplying $\mathbf{G}^{\mathbf{T}}\mathbf{K}^{-\mathbf{1}}$, and the velocity unknowns are eliminated by equation (A2):

$$\mathbf{G}^{\mathbf{T}}\mathbf{K}^{-\mathbf{1}}\mathbf{G}p = \mathbf{G}^{\mathbf{T}}\mathbf{K}^{-\mathbf{1}}f. \tag{A4}$$

The matrix $\mathbf{G}^{\mathbf{T}}\mathbf{K}^{-\mathbf{1}}\mathbf{G}$ on the left hand side is symmetric. This equation is solved with the Conjugate Gradient, *cg*, scheme [*Ramage and Wathen*, 1994].

[30] For the compressible cases, there are two different methods to solve equations (A2) and (A3). In the first method, *iter-cg*, another layer of iterations is added when solving equation (A4). The right-hand side vector is updated by the velocity solution of the previous iteration. This equation can be solved with the same Conjugate Gradient scheme [*Leng and Zhong*, 2008] as the incompressible case:

$$\mathbf{G}^{\mathbf{T}}\mathbf{K}^{-\mathbf{1}}\mathbf{G}p^{(i)} = \mathbf{G}^{\mathbf{T}}\mathbf{K}^{-\mathbf{1}}f - \mathbf{B}u^{(i-1)}. \tag{A5}$$

In the second method, *bicg*, equation (A3) is transformed by premultiplying $(\mathbf{G}^{\mathbf{T}} + \mathbf{B})\mathbf{K}^{-\mathbf{1}}$. The resultant equations become:

$$(\mathbf{G}^{\mathbf{T}} + \mathbf{B})\mathbf{K}^{-\mathbf{1}}\mathbf{G}p = (\mathbf{G}^{\mathbf{T}} + \mathbf{B})\mathbf{K}^{-\mathbf{1}}f. \tag{A6}$$

The matrix $(\mathbf{G}^{\mathbf{T}} + \mathbf{B})\mathbf{K}^{-\mathbf{1}}\mathbf{G}$ on the left hand side is no longer symmetric. This equation can be solved with the Bi-Conjugate Gradient Stabilized scheme

Table B1. Benchmarks for the Compressible Stokes Solver

			Surface Topography		CMB Topography	
Di/γ	η_1	l	Semianalytical	CitcomS	Semianalytical	CitcomS
0	1	2	−0.41919	−0.4191	0.77059	0.7685
0	1	3	−0.43005	−0.4290	0.78466	0.7797
0	1	4	−0.41461	−0.4119	0.73710	0.7295
0	10^4	2	−0.53411	−0.5320	0.32094	0.3207
0	10^4	3	−0.51401	−0.5106	0.35996	0.3589
0	10^4	4	−0.48059	−0.4751	0.38213	0.3794
1.0	1	2	−0.42821	−0.4277	0.74980	0.7375
1.0	1	3	−0.44405	−0.4427	0.75243	0.7485
1.0	1	4	−0.43078	−0.4279	0.69996	0.6932
1.0	10^4	2	−0.53898	−0.5385	0.30622	0.3061
1.0	10^4	3	−0.51932	−0.5162	0.34102	0.3401
1.0	10^4	4	−0.48609	−0.4807	0.36035	0.3579

[*Tan and Gurnis*, 2007]. Both *iter-cg* and *bicg* methods are benchmarked against semianalytical solution in Appendix B and give similar results up to the solver accuracy.

[31] The energy equation is solved using Streamline Upwind Petrov-Galerkin method [*Brooks and Hughes*, 1982]. The composition is tracked by the tracer ratio method [*Tackley and King*, 2003] with the tracer advection routine of *McNamara and Zhong* [2004].

Appendix B: Benchmarks of Semianalytical Solutions

[32] The compressible Stokes solver is benchmarked against semianalytical solutions. Following similar procedure as in the work of *Hager and O'Connell* [1979] and *Zhong and Zuber* [2000], we can expand the spheroidal components of velocity and total stress into spherical harmonics Y_{lm}.

$$\begin{aligned} u_r &= y_1^l Y_{lm} \\ u_\theta &= y_2^l Y_{lm}^\theta \\ u_\phi &= y_2^l Y_{lm}^\phi \\ \tau_{rr} &= y_3^l Y_{lm} \\ \tau_{r\theta} &= y_4^l Y_{lm}^\theta \\ \tau_{r\phi} &= y_4^l Y_{lm}^\phi \end{aligned}, \tag{B1}$$

where y_1^l, y_2^l, y_3^l, and y_4^l are functions of radius only. The and are defined as:

$$\begin{aligned} Y_{lm}^\theta &= \frac{\partial Y_{lm}}{\partial \theta} \\ Y_{lm}^\phi &= \frac{1}{\sin\theta}\frac{\partial Y_{lm}}{\partial \phi} \end{aligned}. \tag{B2}$$

Furthermore, by assuming that the density and its perturbation have the form

$$\begin{aligned} \rho_r &= \exp\left(\frac{Di}{\gamma}(1-r)\right), \\ \delta\rho &= -\rho_r y_t^l Y_{lm} \end{aligned} \tag{B3}$$

and after transformation of variables

$$\begin{aligned} u^l &= \begin{bmatrix} u_1^l & u_2^l & u_3^l & u_4^l \end{bmatrix}^T = \begin{bmatrix} y_1^l & y_2^l & r y_3^l & r y_4^l \end{bmatrix}^T \\ v &= \ln(r) \end{aligned}, \tag{B4}$$

we can write down the continuity and momentum equations as

$$\begin{aligned} \frac{du^l}{dv} &= A^l u^l + b^l \\ A^l &= \begin{bmatrix} -(a+2) & L & 0 & 0 \\ -1 & 1 & 0 & 1/\eta \\ 4\eta(a+3) & -6L\eta & 1 & L \\ -2\eta(a+3) & 2\eta(2L-1) & -1 & -2 \end{bmatrix} \\ b^l &= \begin{bmatrix} 0 & 0 & -Ra\exp\left(\frac{Di}{\gamma}(1-r)\right) r^2 y_t^l & 0 \end{bmatrix}^T \end{aligned}, \tag{B5}$$

where $a = -rDi/\gamma$ and $L = l(l+1)$.

[33] For compressible fluid, the matrix A^l and vector b^l are dependent on r, we therefore cannot get the exact analytical solution from equation (B5) as the propagator matrix method in *Hager and O'Connell* [1979] However, we can still obtain semianalytical solutions by dividing the mantle into many layers and approximating that r is uniform within each layer, which leads to uniform A^l and b^l within each layer. We found that dividing the mantle into 101 uniform layers and expanding the propagator matrix to the 20th order of Taylor expansion are good enough to give accurate solution. We solved for the vertical stresses and horizontal velocities at surface and CMB given free-slip boundary conditions.

[34] The temperature perturbation is a delta function at mid mantle $r = 0.775$. The outer and inner radii of the domain are 1.0 and 0.55, respectively. The Rayleigh number is set to 1.0. These values are chosen to be the same as those used by *Zhong et al.* [2000, Table 1]. The viscosity structure has two layers. The lower layer ($r < 0.8931$) always has a viscosity 1.0. The upper layer has a viscosity η_1 (Table B1). We use 32 elements uniformly distributed in the radial direction in CitcomS. The upper layer spans five elements. The benchmark results are given in Table B1. It should be pointed out that the results of incompressible

cases ($Di/\gamma = 0$) are the same as those given by *Zhong et al.* [2000].

Acknowledgments

[35] E.T. and M.G. have been supported by NSF EAR-0426271. W.L. and S.Z. have been supported by NSF EAR-1015669. The CitcomS code from the Computational Infrastructure for Geodynamics (CIG) was used for this study.

References

Allègre, C., A. Hofmann, and K. O'Nions (1996), The argon constraints on mantle structure, *Geophys. Res. Lett.*, *23*, 3555–3557, doi:10.1029/96GL03373.

Brooks, A. N., and T. J. R. Hughes (1982), Streamline upwind Petrov-Galerkin formulations for convection dominated flows with particular emphasis on the incompressible Navier-Stokes equations, *Comput. Method Appl. Mech. Eng.*, *32*, 199–259, doi:10.1016/0045-7825(82)90071-8.

Burke, K., and T. H. Torsvik (2004), Derivation of large igneous provinces of the past 200 million years from long-term heterogeneities in the deep mantle, *Earth Planet. Sci. Lett.*, *227*, 531–538, doi:10.1016/j.epsl.2004.09.015.

Burke, K., B. Steinberger, T. H. Torsvik, and M. A. Smethurst (2008), Plume generation zones at the margins of large low shear velocity provinces on the core–mantle boundary, *Earth Planet. Sci. Lett.*, *265*, 49–60, doi:10.1016/j.epsl.2007.09.042.

Davaille, A. (1999), Simultaneous generation of hotspots and superswells by convection in a heterogeneous planetary mantle, *Nature*, *402*, 756–760, doi:10.1038/45461.

Davies, G. F. (1999), *Dynamic Earth: Plates, Plumes, and Mantle Convection*, 458 pp., Cambridge Univ. Press, Cambridge, U. K., doi:10.1017/CBO9780511605802.

Deschamps, F., and P. J. Tackley (2009), Searching for models of thermo-chemical convection that explain probabilistic tomography II—Influence of physical and compositional parameters, *Phys. Earth Planet. Inter.*, *176*, 1–18, doi:10.1016/j.pepi.2009.03.012.

Gonnermann, H. M., M. Manga, and A. M. Jellinek (2002), Dynamics and longevity of an initially stratified mantle, *Geophys. Res. Lett.*, *29*(10), 1399, doi:10.1029/2002GL014851.

Gurnis, M. (1986), The effects of chemical density differences on convective mixing in the Earth's mantle, *J. Geophys. Res.*, *91*, 11,407–11,419, doi:10.1029/JB091iB11p11407.

Gurnis, M., C. Hall, and L. Lavier (2004), Evolving force balance during incipient subduction, *Geochem. Geophys. Geosyst.*, *5*, Q07001, doi:10.1029/2003GC000681.

Hager, B. H., and R. J. O'Connell (1979), Kinematic models of large-scale flow in the Earth's mantle, *J. Geophys. Res.*, *84*, 1031–1048, doi:10.1029/JB084iB03p01031.

He, Y., and L. Wen (2009), Structural features and shear-velocity structure of the "Pacific Anomaly," *J. Geophys. Res.*, *114*, B02309, doi:10.1029/2008JB005814.

Hofmann, A. W. (1997), Mantle geochemistry: The message from oceanic volcanism, *Nature*, *385*, 219–229, doi:10.1038/385219a0.

Höink, T., and A. Lenardic (2008), Three-dimensional mantle convection simulations with a low-viscosity asthenosphere and the relationship between heat flow and the horizontal length scale of convection, *Geophys. Res. Lett.*, *35*, L10304, doi:10.1029/2008GL033854.

Huang, J. (2008), Controls on entrainment of a dense chemical layer by thermal plumes, *Phys. Earth Planet. Inter.*, *166*, 175–187, doi:10.1016/j.pepi.2008.01.006.

Ishii, M., and J. Tromp (2004), Constraining large-scale mantle heterogeneity using mantle and inner-core sensitive normal modes, *Phys. Earth Planet. Inter.*, *146*, 113–124.

Ita, J., and S. D. King (1994), Sensitivity of convection with an endothermic phase-change to the form of governing equations, initial conditions, boundary conditions, and equation of state, *J. Geophys. Res.*, *99*, 15,919–15,938, doi:10.1029/94JB00852.

Jellinek, A. M., and M. Manga (2002), The influence of a chemical boundary layer on the fixity, spacing and lifetime of mantle plumes, *Nature*, *418*, 760–763, doi:10.1038/nature00979.

Jellinek, A. M., H. M. Gonnerman, and M. A. Richards (2003), Plume capture by divergent plate motions: Implications for the distribution of hotspots, geochemistry of mid-ocean ridge basalts, and estimates of the heat flux at the core-mantle boundary, *Earth Planet. Sci. Lett.*, *205*, 361–378, doi:10.1016/S0012-821X(02)01070-1.

Lenardic, A., and W. M. Kaula (1994), Tectonic plates, D" thermal structure, and the nature of mantle plumes, *J. Geophys. Res.*, *99*, 15,697–15,708, doi:10.1029/94JB00466.

Leng, W., and S. Zhong (2008), Viscous heating, adiabatic heating and energetic consistency in compressible mantle convection, *Geophys. J. Int.*, *173*, 693–702, doi:10.1111/j.1365-246X.2008.03745.x.

Lowman, J. P., and G. T. Jarvis (1996), Continental collisions in wide aspect ratio and high Rayleigh number two-dimensional mantle convection models, *J. Geophys. Res.*, *101*, 25,485–25,497, doi:10.1029/96JB02568.

Masters, G., G. Laske, H. Bolton, and A. Dziewonski (2000), The relative behavior of shear velocity, bulk sound speed, and compressional velocity in the mantle: Implications for chemical and thermal structure, in *Earth's Deep Interior: Mineral Physics and Tomography From the Atomic to the Global Scale*, *Geophys. Monogr. Ser.*, vol. 117, edited by S. Karato et al., pp. 63–87, AGU, Washington, D. C.

McNamara, A. K., and S. Zhong (2004), Thermochemical structures within a spherical mantle: Superplumes or piles?, *J. Geophys. Res.*, *109*, B07402, doi:10.1029/2003JB002847.

McNamara, A. K., and S. Zhong (2005), Thermochemical structures beneath Africa and the Pacific Ocean, *Nature*, *437*, 1136–1139, doi:10.1038/nature04066.

Nakagawa, T., and P. J. Tackley (2004), Thermo-chemical structure in the mantle arising from a three-component convective system and implications for geochemistry, *Phys. Earth Planet. Inter.*, *146*, 125–138, doi:10.1016/j.pepi.2003.05.006.

Ni, S., E. Tan, M. Gurnis, and D. Helmberger (2002), Sharp sides to the African superplume, *Science*, *296*, 1850–1852, doi:10.1126/science.1070698.

Ramage, A., and A. I. Wathen (1994), Iterative solution techniques for the Stokes and Navier-Stokes equations, *Int. J. Numer. Methods Fluids*, *19*, 67–83, doi:10.1002/fld.1650190106.

Romanowicz, B. (2003), Global mantle tomography: Progress status in the past 10 years, *Annu. Rev. Earth Planet. Sci.*, *31*, 303–328, doi:10.1146/annurev.earth.31.091602.113555.

Sleep, N. H., M. A. Richard, and B. H. Hager (1988), Onset of mantle plumes in the presence of preexisting convection, *J. Geophys. Res.*, *93*, 7672–7689, doi:10.1029/JB093iB07p07672.

Steinberger, B., and T. H. Torsvik (2011), A geodynamic model of plumes from the margins of large low shear velocity provinces, *Geophys. Res. Abstr.*, *13*, EGU2011-3216-1.

Sun, D., D. Helmberger, and M. Gurnis (2010), A narrow mid-mantle plume below southern Africa, *Geophys. Res. Lett.*, *37*, L09302, doi:10.1029/2009GL042339.

Tackley, P. J., and S. D. King (2003), Testing the tracer ratio method for modeling active compositional fields in mantle convection simulations, *Geochem. Geophys. Geosyst.*, *4*(4), 8302, doi:10.1029/2001GC000214.

Tan, E., and M. Gurnis (2005), Metastable superplumes and mantle compressibility, *Geophys. Res. Lett.*, *32*, L20307, doi:10.1029/2005GL024190.

Tan, E., and M. Gurnis (2007), Compressible thermo-chemical convection and application to lower mantle superplumes, *J. Geophys. Res.*, *112*, B06304, doi:10.1029/2006JB004505.

Tan, E., M. Gurnis, and L. Han (2002), Slabs in the lower mantle and their modulation of plume formation, *Geochem. Geophys. Geosyst.*, *3*(11), 1067, doi:10.1029/2001GC000238.

Tan, E., E. Choi, P. Thoutireddy, M. Gurnis, and M. Aivazis (2006), GeoFramework: Coupling multiple models of mantle convection within a computational framework, *Geochem. Geophys. Geosyst.*, *7*, Q06001, doi:10.1029/2005GC001155.

Tan, E., M. Gurnis, L. Armendariz, L. Strand, and S. Kientz (2010), CitcomS user manual, Comput. Infrastruct. for Geodyn., Univ. of Calif., Davis. (Available at http://www.geodynamics.org/cig/software/citcoms)

Thorne, M. S., E. J. Garnero, and S. P. Grand (2004), Geographic correlation between hot spots and deep mantle lateral shear-wave velocity gradients, *Phys. Earth Planet. Inter.*, *146*, 47–63, doi:10.1016/j.pepi.2003.09.026.

To, A., B. Romanowicz, Y. Capdeville, and N. Takeuchi (2005), 3D effects of sharp boundaries at the borders of the African and Pacific superplumes: Observation and modeling, *Earth Planet. Sci. Lett.*, *233*, 137–153, doi:10.1016/j.epsl.2005.01.037.

Torsvik, T. H., M. A. Smethurst, K. Burke, and B. Steinberger (2006), Large igneous provinces generated from the margins of the large low-velocity provinces in the deep mantle, *Geophys. J. Int.*, *167*, 1447–1460, doi:10.1111/j.1365-246X.2006.03158.x.

Torsvik, T. H., K. Burke, B. Steinberger, S. J. Webb, and L. D. Ashwal (2010), Diamonds sampled by plumes from the core-mantle boundary, *Nature*, *466*, 352–355, doi:10.1038/nature09216.

Wang, Y., and L. Wen (2007), Geometry and P- and S- velocity structure of the "African anomaly," *J. Geophys. Res.*, *112*, B05313, doi:10.1029/2006JB004483.

Wen, L. (2001), Seismic evidence for a rapidly varying compositional anomaly at the base of the Earth's mantle beneath the Indian Ocean, *Earth Planet. Sci. Lett.*, *194*, 83–95, doi:10.1016/S0012-821X(01)00550-7.

Wen, L. (2006), A compositional anomaly at the Earth's core-mantle boundary as an anchor to the relatively slowly moving surface hotspots and as source to the DUPAL anomaly, *Earth Planet. Sci. Lett.*, *246*, 138–148, doi:10.1016/j.epsl.2006.04.024.

Zhang, N., S. Zhong, W. Leng, and Z. X. Li (2010), A model for the evolution of the Earth's mantle structure since the Early Paleozoic, *J. Geophys. Res.*, *115*, B06401, doi:10.1029/2009JB006896.

Zhong, S., and B. H. Hager (2003), Entrainment of a dense layer by thermal plumes, *Geophys. J. Int.*, *154*, 666–676, doi:10.1046/j.1365-246X.2003.01988.x.

Zhong, S., and M. T. Zuber (2000), Long-wavelength topographic relaxation for self-gravitating planets and implications for the time-dependent compensation of surface topography, *J. Geophys. Res.*, *105*, 4153–4164, doi:10.1029/1999JE001075.

Zhong, S. J., M. T. Zuber, L. N. Moresi, and M. Gurnis (2000), Role of temperature dependent viscosity and surface plates in spherical shell models of mantle convection, *J. Geophys. Res.*, *105*, 11,063–11,082, doi:10.1029/2000JB900003.

Zhong, S., N. Zhang, Z. Li, and J. H. Roberts (2007), Supercontinent cycles, true polar wander, and very long-wavelength mantle convection, *Earth Planet. Sci. Lett.*, *261*, 551–564, doi:10.1016/j.epsl.2007.07.049.

Zhong, S., A. McNamara, E. Tan, L. Moresi, and M. Gurnis (2008), A benchmark study on mantle convection in a 3-D spherical shell using CitcomS, *Geochem. Geophys. Geosyst.*, *9*, Q10017, doi:10.1029/2008GC002048.